Assessment of the Thin-airfoil Method for Predicting Steady Pressure Distribution on Partially-porous Airfoils

Luesutthiviboon, Salil; Avallone, Francesco; Ragni, Daniele; Snellen, Mirjam

DOI
10.2514/6.2019-2647

Publication date
2019

Document Version
Final published version

Published in
25th AIAA/CEAS Aeroacoustics Conference

Aeroacoustics Conferences
20-23 May 2019, Delft, The Netherlands
25th AIAA/CEAS Aeroacoustics Conference

10.2514/6.2019-2647

Assessment of the Thin-airfoil Method for Predicting Steady Pressure Distribution on Partially-porous Airfoils

Salil Luesutthiviboon*, Daniele Ragni†, Francesco Avallone‡, and Mirjam Snellen§
Faculty of Aerospace Engineering, Delft University of Technology, 2629 HS Delft, The Netherlands

An analytical method for predicting the steady pressure distribution on porous airfoils with a prescribed porosity distribution is assessed through comparison of its lift prediction with experimental data. The method is based on the thin-airfoil formulation. The no-slip boundary condition of the airfoil surface has been replaced by the Darcy's boundary condition, allowing interaction of the air flow between the suction and the pressure sides. The 'PARSEC' airfoil parameterization method is employed to minimize inaccuracies in modelling the airfoil shape. A general match is found between model predictions and measurements of fully- and partially-porous airfoils, given that the airfoil is thin and/or the porous materials used have relatively high air flow resistivities (r). However, a difference between model predictions and measurements occurs for partially porous airfoils with low chordwise porous extent ratios (c_p/c), or with a relatively low r. The model gives a drop of pressure difference on the solid extent upstream of the porous extent, which is not found in the measurements. This may lead to an underestimation of lift by the model. Apart from that, prediction inaccuracies could also be expected for airfoils with a relatively high surface curvature and/or thickness.

Nomenclature

A	=	cross-sectional area of material sample [m^2]	c	=	chord length [m]
c_l	=	lift coefficient [-]	c_p/c	=	chordwise ratio of porous extent [-]
C	=	porosity coefficient [m^4(Ns)$^{-1}$]	d	=	thickness of porous material sample [m]
$d(x)$	=	local thickness of the airfoil [-]	F_L	=	lift force [N]
$g(u)$	=	generic function [-]	$\hat{i}$, $\hat{n}$	=	unit vectors in x and normal to camber line [-]
p	=	static pressure [Pa]	$p'(x)$	=	local dimensionless static pressure difference [-]
P	=	porosity [-]	q	=	volumetric flow rate [m^{3}s^{-1}]
r	=	air flow resistivity [Nsm^{-4}]	$R(x)$	=	local porosity distribution [-]
s	=	span [m]	S	=	airfoil wetted area [m^2]
$u(x)$	=	local flow velocity [m/s]	$\mathbf{V}$	=	background velocity vector [m/s]
V_∞	=	free-stream velocity [m/s]	w_s	=	local flow velocity [m/s]
x, z	=	horizontal and vertical axes [-]	z_a	=	camber line [-]
α	=	angle of attack [rad]	δ	=	porosity constant [m]
$\gamma(x)$	=	local vortex strength [-]	ϕ	=	potential flow field [-]
ρ	=	fluid density [kgm^{-3}]	$\psi(u)$	=	generic function [-]

The symbols used in the Appendix are excluded.

*PhD Candidate, Section Aircraft Noise and Climate Effects (ANCE), Department of Control and Operations (C&O)
†Assistant Professor, Department of Aerodynamics, Wind Energy, Flight Performance and Propulsion (AWEP)
‡Assistant Professor, Department of Aerodynamics, Wind Energy, Flight Performance and Propulsion (AWEP)
§Associate Professor, Section Aircraft Noise and Climate Effects (ANCE), Department of Control and Operations (C&O)

I. Introduction

Porous airfoils are designed aiming to reduce airfoil self-noise, especially the turbulent boundary layer trailing-edge noise [1]. The usage of porous materials on airfoils has been inspired by the wings of owls, which are able to make a relatively silent flight [2]. This is because their permeable feathers, i.e. having a finite impedance, allow communication between the two sides of the wings, thus damping the mismatch of pressure fluctuation between the suction and the pressure sides before the flow reaches the trailing-edge [3]. This damping then lowers its acoustic scattering [4–6].

Many researchers have experimentally measured noise emission from fully-[2, 7, 8] and partially-[4, 5, 9–12] porous airfoils. It has been widely shown that the porous airfoils are able to achieve a considerable noise reduction, compared to the solid counterpart. For example, Geyer et al. [2, 7] showed that noise emitted by a fully-porous SD7003 airfoil could be attenuated up to 8 dB over a large frequency range below $\sim$8 kHz.

Despite the noise reduction capability, many researchers have also experimentally shown that lift generated by porous airfoils could reduce with increasing porosity [2, 9, 11–14], due to the fact that the static pressures on the suction and the pressure sides are able to communicate and balance through the permeable material [2]. In a recent measurement done by Aldheeb et al. [13], who measured lift produced by thin fully- and partially-porous airfoils by means of wind-tunnel measurements, lift reduction of 13% has been found at the angles of attack above 10 degrees. Similarly, Geyer et al. [2, 9, 12] measured the lift produced by a fully-porous SD7003 airfoil in an open-jet wind tunnel. They found up to 75% reduction of lift force at the (geometrical) angles of attack between -12 and 24 degrees, when the airfoil was made of a highly-porous 'M-Pore' material. This downside makes porous airfoils less appealing for practical usages, such as for wind turbine blades. Therefore, it has been strongly suggested by Hajian and Jaworski [15] that the aerodynamic performance of the porous airfoils should be investigated carefully, as well as the noise reduction aspects.

Some attempts to minimize the adverse effect of incorporating porous materials on airfoils on the lift have been made. One commonly-used approach is to design a partially-porous airfoil, i.e. limiting the application of the porous materials only close to the trailing-edge and finding an optimal chordwise porous extent length which can effectively reduce the noise emission while maintaining the aerodynamic performance [4, 5, 9–12, 16]. Recent experimental work by Geyer et al. [9, 12] extended the aforementioned lift and noise measurements of a fully-porous SD7003 airfoil to a series of partially-porous SD7003 airfoils with different chordwise porous extent percentages. It has been found that when a porous 'Recemat' material was used, a noise reduction of approximately 5 to 10 dB at low to medium chord-based Strouhal numbers could be preserved while limiting the chordwise extent percentage of the porous material to only 5 to 10% in the region close to the trailing-edge. Additionally, a substantial amount of lift force could be recovered, compared to the fully-porous airfoil with the same porous material [9, 12]. Interestingly, a close investigation of the static pressure distribution on the solid extent of the partially-porous NACA0018 airfoil by Rubio Carpio et al. [4] showed that the application of the porous materials hardly affects the static pressure distribution upstream, even when the effective angle of attack was varied up to approximately 6.8 degrees. This suggests that the lift loss is localized only to the porous region. These recent experimental investigations have given an implication that there is the possibility to minimize the lift penalty while maintaining or maximizing noise reduction ability of the partially porous airfoils by optimally designing the chordwise porous extent ratio and the porosity distribution along the chord.

However, a very limited number of prediction tools for predicting the pressure distribution on porous airfoils, which could help designing the optimal porous airfoil, is currently available. In addition, the performance of those tools, e.g. by comparing the results to experimental or numerical results, has not yet been extensively investigated. Iosilevskii [17, 18] has developed a closed-form expression to predict the aerodynamic parameters of a thin airfoil having a finite porous extent including the pressure distribution and the lift. The Darcy's law was applied to determine the possible flow velocity through the porous extent, based on the porous material's properties. With increasing porosity, a reduction of the lift slope and a displacement of the airfoil's aerodynamic center have been found. Hajian and Jaworski [15] have extended the model of Iosilevskii to predict the steady pressure distribution and lift coefficient of porous airfoils having porosity gradients, i.e. porosity defined as a differentiable function along the chord. This extension enables modelling different porous material thicknesses or properties along the chord. The predictions have been compared with the experimental results from the fully-porous SD7003 airfoil (Geyer et al. [2]). Hajian and Jaworski studied the variation of the airfoil's lift coefficient with the porosity constant δ, a parameter that increases with increasing porosity. The actual and predicted lift coefficients agreed up to a certain value of porosity constant slightly above zero. The the model was found to underestimate the lift for the porosity constants higher than 0.01. This can result from, for example, 1.) the inherent uncertainty of the effective angle of attack as the measurement was performed in an open-jet wind tunnel [2, 9, 12], 2.) the inaccuracy in fitting the airfoil's camber line and thickness distribution with a polynomial curve, and 3.) the assumption regarding the Darcy's boundary condition, which may not fully explain how some porous materials effectively interact with the air flow when installed on an airfoil [15]. Another recent comparison has been

done by Aldheeb et al. [13] on their own experimental results of a fully-porous wing. They also found that the trend of the reducing lift curve slope with the increasing porosity given by the thin-airfoil method matched qualitatively well with the experimental data.

In this paper, the method for predicting the steady pressure distribution on porous airfoils of Hajian and Jaworski is further assessed, by comparing the prediction of the lift coefficient and lift curve slope to recent experimental datasets focusing on partially-porous airfoils. An alternative method for parameterizing the airfoil's geometry, namely the 'PARSEC' method [19], is used instead of the polynomial curve fitting of the camber line. In this way, the actual surface curvature of the airfoil is accurately parameterized by a set of differentiable functions, which can also be used in other numerical methods for further comparison. Use is made of the experimental data of a thin and symmetric partially-porous airfoil from Aldheeb et al. [13] and the fully- and partially-porous SD7003 airfoil from Geyer et al. [2, 9, 12]. For both of the datasets, lift data are available for various chordwise porous extent ratios.

This manuscript is structured as follows: Section II explains the theory and assumptions used in formulating an equation for predicting the non-dimensionalized static pressure difference on an arbitrary porous airfoil of Hajian and Jaworski. The experimental datasets used are explained in Section III. Section IV presents the results and discussions.

II. Thin-airfoil Method for Predicting Steady Pressure Distribution

Hajian and Jaworski [15] have derived an expression for the non-dimensionalized steady static pressure difference between the suction and the pressure sides as a function of the chordwise location for porous airfoils. Their work is an extension to the expression derived by Iosilevskii [17, 18], enabling the pressure distribution to be solved for any arbitrary porosity distribution specified as a differentiable function of the chordwise location [15]. The governing equations and main assumptions of Hajian and Jaworski are presented in this section. However, the detailed steps for solving the Riemann-Hilbert integral problem [20, 21] are omitted for conciseness. Interested readers are referred to [15] for the full derivation.

Consider a potential flow field ϕ in the x-z space depicted in Fig. 1 where there exists a background flow velocity field of $|\mathbf{V}| = V_\infty$ directed along the x axis, i.e. $\mathbf{V} = \begin{bmatrix} V_\infty & 0 \end{bmatrix}^T$. The background flow velocity is perturbed by an airfoil located within this velocity field. The camber line of the airfoil is represented by z_a. The thin airfoil theory represents the airfoil's perturbation of the background flow velocity by vortices of different strengths $\gamma(x)$ distributed along the x axis. The local vortex strength represents the velocity difference between the suction and the pressure sides of the airfoil as $\gamma(x) = u_S(x) - u_P(x)$ [22]. This can be linked to the mismatch of the static pressures between the suction and the pressure sides, which is of interest for predicting the lift of the airfoil, by the Bernoulli's equation [22]. Let $p'(x)$ be the static pressure difference between the suction and the pressure sides, non-dimensionalized by the dynamic pressure, $p'(x)$ is related to $\gamma(x)$ as follows [15]

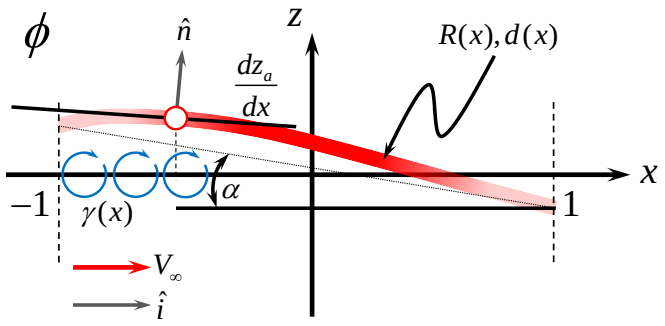

Fig. 1 Schematic of a thin airfoil with a prescribed chordwise porosity and thickness distribution subjected to the free-stream flow used in the thin-airfoil method for predicting steady pressure distribution (adapted from [17, 18]).

$$p'(x) = \frac{p_S(x) - p_P(x)}{\frac{1}{2}\rho V_\infty^2} = -2\frac{\gamma(x)}{V_\infty}, \tag{1}$$

Let $\hat{n}$ be a vector normal to the local airfoil's camber line such that $\hat{n} = \begin{bmatrix} -dz_a/dx & 1 \end{bmatrix}^T$. Typically, for impermeable airfoils, the velocity component in this direction should be zero. However, for porous airfoils, a small local flow velocity w_s is allowed. The boundary condition is re-defined as [23]

$$w_s = (\nabla\phi + \mathbf{V})^T \cdot \hat{n} = \left(\begin{bmatrix} \frac{\partial\phi}{\partial x} \\ \frac{\partial\phi}{\partial z} \end{bmatrix} + \begin{bmatrix} V_\infty \\ 0 \end{bmatrix} \right)^T \cdot \begin{bmatrix} -\frac{dz_a}{dx} \\ 1 \end{bmatrix}. \tag{2}$$

It is required that w_s is small compared to V_∞, as well as the local slope of the airfoil. Having imposed the aforementioned assumptions and neglecting the higher-order terms, Eq. (2) becomes [15]

$$\frac{\partial\phi}{\partial z} = w_s + V_\infty \frac{dz_a}{dx}, \tag{3}$$

where the solution for the z-component of the potential flow $\partial\phi/\partial z$ is [22]

$$\frac{\partial\phi}{\partial z} = -\frac{1}{2\pi} \int_{-1}^{1} \frac{\gamma(\xi)}{x-\xi} d\xi. \tag{4}$$

To close the formulation of the problem, the local flow velocity is assumed to follow the Darcy's boundary condition [24, 25], which states that the local flow velocity is a function of the static pressure difference, the porous medium, and the fluid property. We have

$$w_s(x) = -CR(x)(p_S(x) - p_P(x)), \tag{5}$$

where C is the porosity coefficient and $R(x)$ is the porosity distribution. In relation to the fluid property and the porous material thickness, C is the inverse of the air flow resistivity provided by the porous material, and $R(x)$ is the inverse of the local porous material thickness [15] (see Section III.B).

By substituting Eqs. (5) and (4) into Eq. (3), and using the relationship between $p'(x)$ and $\gamma(x)$ as in Eq. (1), Eq. (3) is rearranged as

$$\rho V_\infty CR(x)p'(x) - \frac{1}{2\pi} \int_{-1}^{1} \frac{p'(t)}{t-x} dt = 2\frac{dz_a}{dx}. \tag{6}$$

Equation (6) is formulated as a Riemann-Hilbert problem [20, 21] and solved (see Section 3 of [15] for more details). Finally, the solution for $p'(x)$ is formulated as

$$p'(x) = \frac{4\psi(x)}{1+\psi^2(x)} \frac{dz_a}{dx} - \frac{4}{\pi\sqrt{1+\psi^2(x)}} \exp\left(\int_{-1}^{1} \frac{g(\psi(t))}{t-x} dt \right) \cdot \int_{-1}^{1} \frac{dz_a/dt}{\sqrt{1+\psi^2(t)} \exp\left[\int_{-1}^{1} (g(\psi(\xi))/(\xi-t)) d\xi \right] (x-t)} dt, \tag{7}$$

where $\psi(x) = 2\rho V_\infty CR(x)$, and $g(\psi(x)) = (1/\pi)\cot^{-1}\psi(u)$.

Having obtained the non-dimensionalized static pressure difference $p'(x)$, the lift coefficient c_l is calculated by integrating $p'(x)$ along the chord [15] as

$$c_l = -\frac{1}{2} \int_{-1}^{1} p'(x) dx. \tag{8}$$

III. Experimental Lift Data of Porous Airfoils

A. Thin and symmetric airfoil

Aldheeb et al. [13] performed an extensive experimental campaign to measure aerodynamic forces, namely, lift, drag, and pitching moment, on porous airfoils and wings using a six-component force balance. In the current paper, only the dataset of the partially-porous airfoil is considered. The thin airfoil profile with a thickness-to-chord ratio of 3.6% was installed in a closed-section wind tunnel. The free-stream flow speed was set to 20 m/s, which corresponds to a chord-based Reynolds number of 3.45×10^5. The tests were carried out up to the maximum angle of attack of 14 degrees.

Honeycomb grids were used to create porosity, i.e. the small channels on the honeycomb connected the suction and the pressure sides. Aldheeb et al. used the geometry-based parameter, porosity P, to characterize the porous material. Different porosities were obtained by covering some channel openings on the honeycomb to vary the number of the voids. The porosity was then defined as the ratio between the void volume and the total volume as [13]

$$P = \frac{\text{void volume}}{\text{total volume}}. \tag{9}$$

Note that this geometry-based characterization method differs from another frequently-used method for characterizing porous materials [2, 4, 5, 9, 12] which subjects a porous material sample to a static pressure difference to measure the air flow resistivity (see Section III.B for further details).

For the thin-airfoil case, porosity was applied only to the trailing-edge region by covering all the honeycomb channel openings on the airfoil surface upstream up to various chordwise extents [13]. In the current manuscript, a parameter $c_p/c \in [0, 1]$ is defined to represent the chordwise ratio of the porous extent, with $c_p/c = 0$ and 1 meaning fully-solid and fully-porous airfoils, respectively.

B. SD7003 airfoil

Another experimental dataset used for comparison in this paper is from the experimental works of Geyer et al. on fully- [2] and partially-porous [9, 12] SD7003 airfoils. The airfoil model with a chord of $c = 0.235$ m, and a span of $s = 0.4$ m, made of many different porous materials was installed in an open-jet aeroacoustic wind tunnel. The lift and drag forces were measured by a six-component force balance. The free-stream flow speed was varied between 18 and 87 m/s, corresponding to a chord-based Reynolds number of 2.8×10^5 to 1.35×10^6, and a Mach number of 0.05 to 0.25 [9, 12, 15]. The geometrical angle of attack was varied between -12 and 24 degree. It is important to note that the effective angle of attack could substantially deviate from the geometrical angle of attack since the airfoil was subjected to the unbounded flow. Due to the experimental setup, it was not possible to perform corrections for the angle of attack [2, 15]. Apart from that, the span of the airfoil model was larger than the diameter of the jet nozzle of 0.2 m. This suggests that only a fraction of the total airfoil area S was the wetted area.

Since there is no detailed data of the surface pressure distribution, only the resulting lift coefficient is compared to the prediction given by the thin-airfoil method, i.e. Eq. (8). Let F_L be the measured lift force, the lift coefficient is then calculated by [9, 15]

$$c_l = \frac{2F_L}{\rho V_\infty^2 cs} = \frac{2F_L}{\rho V_\infty^2 S}, \tag{10}$$

given that the values of s or S used are the effective values [9, 26], due to the aforementioned reasons.

The porous materials were characterized by measuring their air flow resistivities r, according to the ISO 9053 standard [27]. The air flow resistivity was determined from the static pressure drop Δp across a porous material sample with the cross-sectional area A and the thickness d, when the sample was subjected to the volumetric air flow rate q as [2, 9, 12, 15]

$$r = \frac{\Delta pA}{qd}. \tag{11}$$

As a link to the model, $q/A = w_s$ in Eq. (5), and $C = 1/r$ [15]. The material details are given in Table 1. Some important remarks regarding the usage of r were given by Geyer et al. [9, 12]. First, the values of r obtained by the aforementioned characterization settings may not fully describe exactly how the material interacts with the air flow when it is integrated to the airfoil. Second, the airfoil manufacturing process may have caused the effective pore sizes on the surface to differ from those in the material samples, leading to the different effective r. Therefore, care must be taken when incorporating the measured r to compare the aerodynamic (and also acoustic) results from the different porous materials obtained from various sources.

In the recent experimental campaign of Geyer et al. [9, 12], partially-porous airfoils were also investigated as well as fully-porous airfoils. The porous extent of the airfoil was limited only to the trailing-edge region by covering the remaining part of the airfoil with a thin impermeable sheet [9, 12]. Airfoils with various porous extents were investigated. Again, the chordwise ratio of the porous extent is denoted as c_p/c. In the present manuscript, lift data of partially-porous airfoils made of 'Recemat' having $r = 8,200$ Nsm^{-4} (see Table 1) is presented, same as presented in [9, 12]. Lift data of airfoils made of the remaining materials tabulated in Table 1 are presented only for $c_p/c = 1$.

Table 1 Porous material data used in this manuscript (adapted from [2, 9, 12]). The given plot markers are used in Fig. 6.

Name	Air flow resistivity r [Nsm^{-4}]	Plot marker
Reference	∞	✳
Recemat	8,200	▽
Damtec USM	12,900	□
Damtec estra	86,100	◇
Siperm R200	150,000	▷
Porex	316,500	△

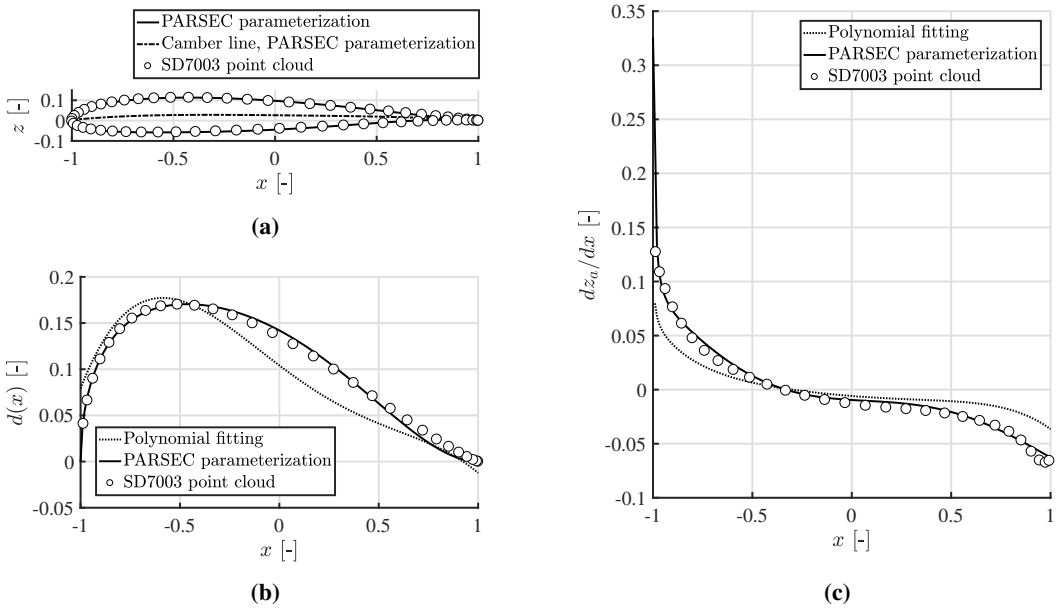

Fig. 2 Parameterization of the SD7003 airfoil using the PARSEC method: (a) the PARSEC airfoil compared to the point cloud of the SD7003 airfoil, (b) the chordwise thickness distribution $d(x)$, and (c) the local slope of the camber line dz_a/dx, derived from the PARSEC parameterization.

As mentioned in Section II, the airfoil's local thickness $d(x)$ is incorporated in the chordwise porosity distribution $R(x)$ as $R(x) = 1/d(x)$ [15]. In this work, the geometry of the airfoil is parameterized using the 'PARSEC' method [19], which is a dedicated method for airfoil parameterization describing the upper and lower surfaces of the airfoil using two explicit PARSEC polynomial equations based on the user-defined airfoil design variables. The local airfoil thickness $d(x)$ and the slope of the camber line with respect to the free-stream flow direction dz_a/dx can directly be derived from the PARSEC polynomial equations. The detailed explanation of the method, including the values of the PARSEC design variables, and the PARSEC polynomial coefficients for the SD7003 airfoil are given in the Appendix. The parameterized SD7003 airfoil and the derived quantities used as inputs for the thin-airfoil method, namely, $d(x)$ and dz_a/dx are shown in Figs. 2a to 2c. It can be seen that the PARSEC method allows a more accurate representation of the airfoil's actual geometry than the typical polynomial curve fitting. This is quantified by the values of the sum of squared differences (SSD) between the parameterized $d(x)$ and dz_a/dx, and those obtained from the airfoil point cloud presented in Table 2. It can be seen that the SSDs achieved by the PARSEC parameterization method for both $d(x)$ and dz_a/dx are well below those achieved by the polynomial curve fitting.

Table 2 Sum of squared differences (SSD) between the parameterized $d(x)$ and dz_a/dx and those obtained from the airfoil point cloud for the polynomial fitting and PARSEC parameterization methods.

Parameter	Polynomial curve fitting	PARSEC parameterization
$d(x)$	128.98×10^{-4}	6.10×10^{-4}
dz_a/dx	165.88×10^{-4}	15.17×10^{-4}

IV. Results and Discussion

In order to allow for a consistent comparison with the previous work by Hajian and Jaworski, the porosity constant δ is employed as a parameter describing the interaction between the fluid and the porous material as [15]

$$\delta = \rho V_\infty C = \frac{\rho V_\infty}{r}. \tag{12}$$

Figure 3a (adapted from [13]) shows the experimentally-obtained lift curve slopes $c_{l\alpha}$ of a thin and symmetric airfoil having different chordwise porous extent ratios c_p/c, normalized by the maximum lift curve slope $c_{l\alpha,\max}$, as functions of porosity P^2. The slopes were calculated for angles of attack between 2 and 8 degrees [13]. As an attempt to compare the results in Fig. 3a to the prediction from the thin-airfoil method, Fig. 3b shows the predicted normalized lift curve slope values $c_{l\alpha}/c_{l\alpha,\max}$ of the thin and symmetric airfoil having the same c_p/c values to those shown in 3a. Correspondingly, the angles of attack used in this calculation lie between 2 and 8 degrees. For a symmetric airfoil as in this case, the angle of attack α can simply be defined in the model by setting the term dz_a/dx in Eq. (7) to $-\alpha$ [15].

As mentioned previously, the porosity P represents the geometrical characteristic of the honeycomb, while the parameter δ employed by the thin-airfoil model is based on the air flow resistivity r, which is acquired experimentally as described in Section III.B. One way to approximate r from the geometry of the porous material is by using the Ergun's equation [28], which models the porous material as a space packed by small spheres. One needs to come up with an equivalent sphere diameter value that best represents the geometry of the porous material of interest [29]. However, in the current work, it is motivated not to introduce additional uncertainties by attempting to model r of the honeycomb. Therefore, Figs. 3a and 3b are shown separately and a qualitative comparison is made.

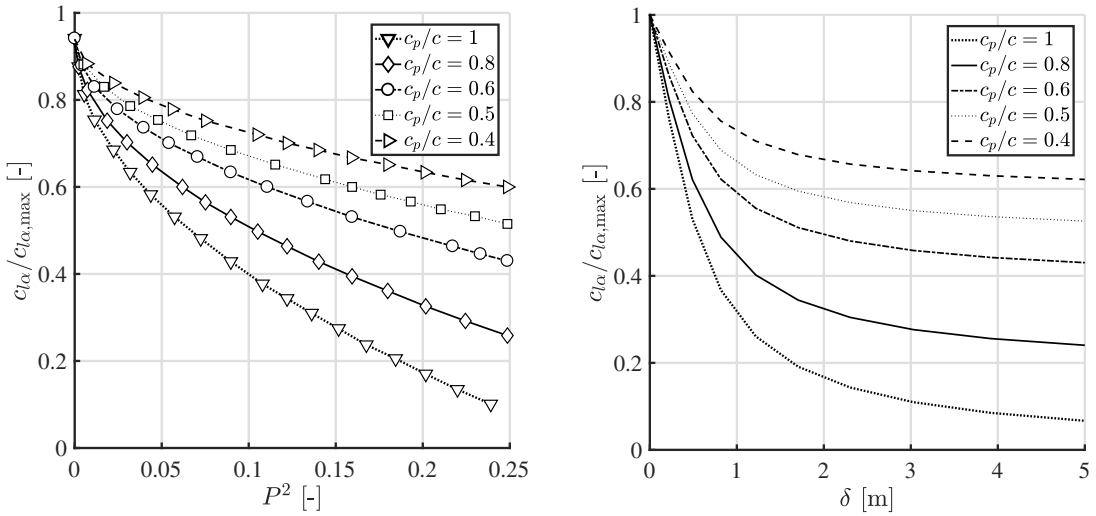

(a) **(b)**

Fig. 3 Normalized lift curve slope $c_{l\alpha}/c_{l\alpha,\max}$ of a symmetric thin airfoil for various chordwise porous extent ratios c_p/c obtained (a) experimentally (adapted from [13]) and (b) from the thin-airfoil method. The values of $c_{l\alpha}/c_{l\alpha,\max}$ are shown versus (a) porosity P^2 and (b) porosity constant δ.

It can be seen that both the experimental and modelled $c_{l\alpha}/c_{l\alpha,\max}$ drop consistently with the increasing c_p/c. For example, the reduction of $c_{l\alpha}/c_{l\alpha,\max}$ when c_p/c increases from 0.6 to 0.8 is approximately twice as much as the

reduction when c_p/c increases from 0.5 to 0.6. Noticeably, for the low values of porosity and porosity constant, the reduction of lift appears to be more sensitive to the increasing porosity compared to the relatively high values of porosity. This is indicated by the gradually-decreasing slope of $c_{l\alpha}/c_{l\alpha,\max}$ with increasing P^2 and δ.

Further investigation is presented in Figs. 4a and 4b, where the distributions of $-p'(x)$ are presented for the angles of attack of 2 and 8 degrees, respectively. The different values of c_p/c are consistent to those presented in Figs. 3a and 3b. Here, δ is taken as 1.

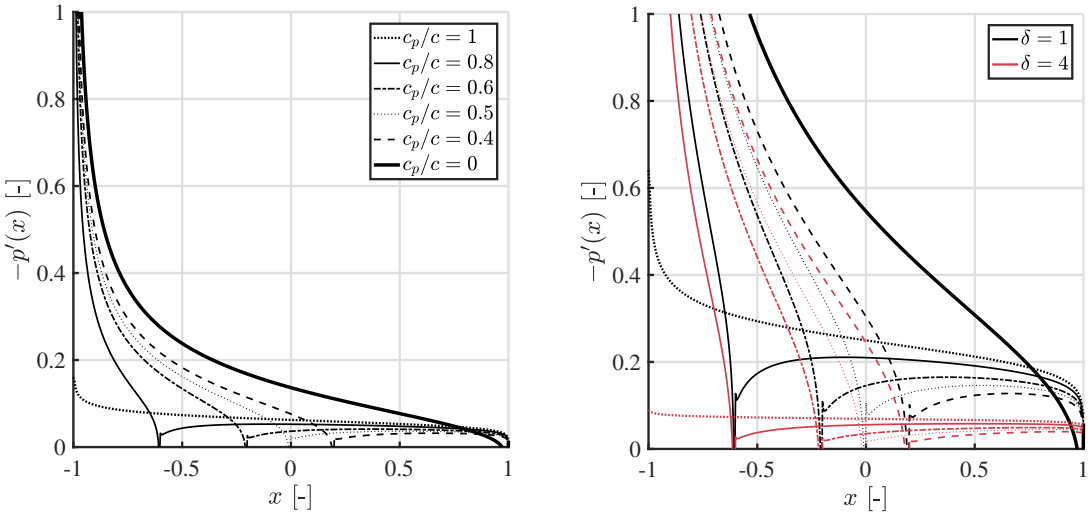

(a) **(b)**

Fig. 4 Predicted distribution of the dimensionless static pressure difference $-p'(x)$ along the chord x of a symmetric airfoil for various chordwise porosity extent ratios c_p/c, taking (a) α = 2 degrees and δ = 1 and (b) α = 8 degrees and δ = 1 and 4.

Interestingly, when the porous extent is limited only to a certain chordwise extent of the airfoil, a substantial drop of $-p(x)$ is also found upstream above the solid part of the airfoil. This however contradicts to the recent experimental findings of Rubio Carpio et al. [4] which found that the pressure distribution on partially-porous airfoil above the upstream solid extent is hardly affected by the integration of the porous materials. This peculiar drop of $-p'(x)$ could attribute to the rapid drop of lift for the low porosity values just above zero seen in Fig. 3b. The effects of porosity is further assessed in Fig. 4b where the prediction of $-p'(x)$ for $\delta = 4$ is also given. When δ increases from 1 to 4, the reduction of $-p'(x)$ upstream of the porous extent is not as large as when δ increases from 0 to 1. Instead, the majority of $-p'(x)$ reduction is observed on the porous extent itself. This could attribute to the more gradual drop of lift for the relatively higher values of δ. The behavior observed so far implies that, due to the overestimation of $-p'(x)$ drop upstream of the porous extent for partially-porous airfoils, the thin-airfoil model may underpredict the lift of partially-porous airfoils, when compared against experimental data.

Next, the thin-airfoil method is applied to predict the pressure distribution on a cambered airfoil. Figure 5 shows the predicted distribution of $-p'(x)$ along the chord of the SD7003 airfoil for various porosity constants δ, taken to be consistent to those presented in Fig. 4 in [15]. The results for the fully-porous airfoil (c_p/c = 1) are shown by the dashed lines, and the partially-porous airfoil with c_p/c = 0.2 are shown by the thin solid lines with the corresponding colors. The values of $-p'(x)$ predicted by the panel method in XFOIL [30], assuming inviscid flow are also plotted.

Considering the reference airfoil case ($\delta = 0$ and $c_p/c = 0$), the shape of $-p'(x)$ is similar to that given by XFOIL. The mismatch is found close to the leading-edge, up to approximately 50% of the chord. The main reason for this mismatch is because of the relatively high surface curvature and the maximum thickness-to-chord ratio of the SD7003 airfoil around this region (see Fig. 2a). The actual shape of the airfoil is taken into account in the panel method of XFOIL while only the camber line is used in the thin-airfoil method. Therefore, one would expect inaccuracies of the thin-airfoil method when applied to airfoils with the distinct surface curvature and thickness.

As the porosity constant δ increases, the difference of the static pressure between the suction and the pressure sides

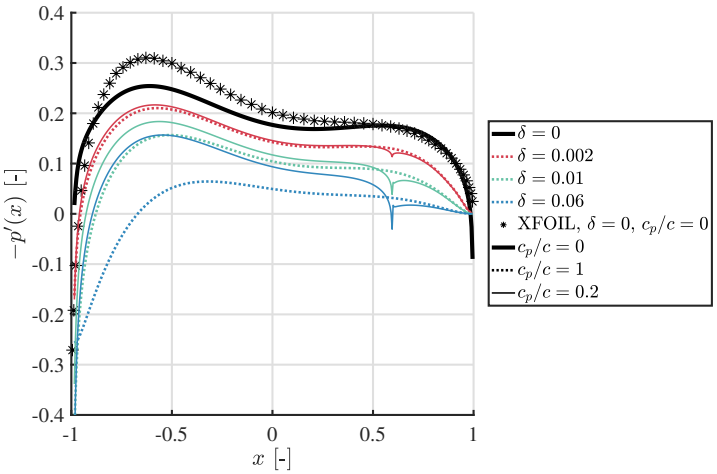

Fig. 5 Predicted distribution of the dimensionless static pressure difference $-p'(x)$ along the chord x of an SD7003 airfoil for various porosity constants δ.

of the airfoil reduces, indicated by the downward shifting of the $-p'(x)$ curve. The trend agrees well with Fig. 4 in [15], including the downstream shift of the zero-crossing point when δ increases. This indicates that when the airfoil is fully porous, the produced pressure difference is weaker than that of the reference solid airfoil. The absolute values of $-p'(x)$ in Fig. 5 may not be exactly the same as that presented by Hajian and Jaworski. This is due to the PARSEC airfoil geometry parameterization method which is employed in this paper instead of the polynomial fitting method.

When the porous extent of the airfoil is limited only to 20% of the chord close to the trailing-edge, a slightly different trend of $-p'(x)$ is observed. First, at the junction between the solid and the porous extent, a drop of $-p'(x)$ is found. This could represent the local mean flow acceleration which occurs on the pressure side, as the flow on the pressure side is allowed to interact with the lower-pressure region on the suction side through the porous material. A stronger $-p'(x)$ drop is observed as δ increases. Interestingly, the downward shift of the $-p'(x)$ seems to be less affected by the increasing δ. This could imply that, by limiting the porous region to only close to the trailing-edge of the airfoil, the sensitivity of lift reduction with the increasing porosity could be reduced. This agrees with the finding of Aldheeb et al. [13] who found that, for airfoils with regional porosity (only close to the trailing-edge), one needs to apply a porous material with a higher porosity, in order to reach a similar reduction of lift compared to airfoils with distributed porosity (fully-porous). Again, the reduction of $-p'(x)$ on the solid extent upstream of the porous extent is still observed in this case.

Figure 6 compares the predicted c_l versus δ for the fully-($c_p/c = 1$) and the partially-($0 < c_p/c < 1$) porous SD7003 airfoil with the recent experimental data of Geyer et al. [9, 12]. The porous material used in the partially-porous airfoils was 'Recemat' ($r = 8,200$ Nsm^{-4}), indicated by $\triangledown$ in the plot. The different marker face colors represent the different values of c_p/c which correspond to the color of the curves. The white markers mean that the airfoil is made entirely of that certain porous material, i.e. $c_p/c = 1$. All the experimental data points shown were measured at the geometrical angle of attack of 4 degrees. The effective angle of attack is unknown due to the aforementioned uncertainties. However, the effective angle of attack is taken as -0.8 degree in the thin-airfoil prediction, and the lift coefficients are presented relative to the maximum value, i.e. $c_l - c_{l,\max}$. Therefore, only the relative trend between the prediction and the experimental data is discussed.

Consider the enlarged area in Fig. 6 for the low values of δ where the fully-porous airfoil data are concentrated. Seemingly, the trend of c_l reduction for most of the porous materials follows the trend given by the corresponding prediction using $c_p/c = 1$ relatively well, compared to outside the enlarged region. The trend of the 'Porex' airfoil data which has the highest value of r of 316,500 Nsm^{-4} best agrees with the prediction for $c_p/c = 1$, followed by 'Damtec estra' ($r = 86,100$ Nsm^{-4}) and 'Sriperm' ($r = 150,000$ Nsm^{-4}). Note that the ranking of the lift reduction does not fully follow the ranking r. For example, the reduction of lift given by 'Sriperm' ($r = 150,000$ Nsm^{-4}) is lower than that of 'Porex' ($r = 316,500$ Nsm^{-4}), although 'Sriperm' is characterized to have a relatively lower r. This could be because, when the material is shaped by a water jet to an airfoil, some pores might have been closed, leading to a new effective air flow resistivity as remarked in [9, 12].

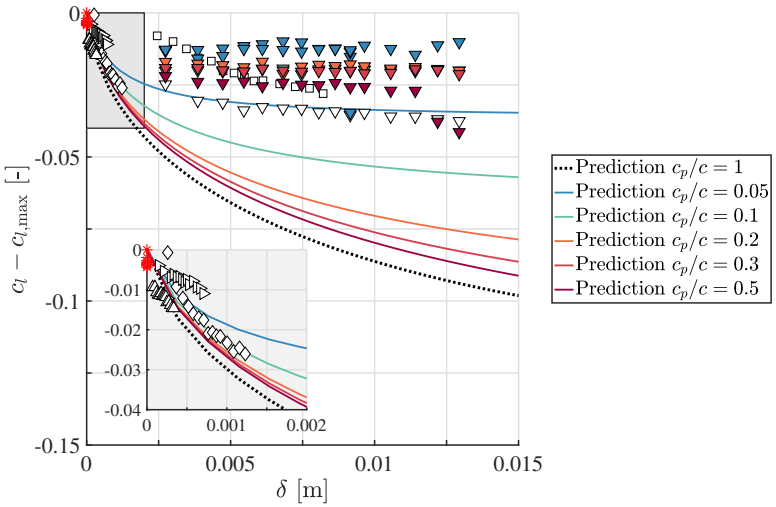

Fig. 6 Lift coefficients c_l versus porosity constants δ predicted by the thin-airfoil method for fully- and partially-porous airfoils having different chordwise porous extent ratios c_p/c, compared to the experimentally-measured c_l of various fully-porous airfoils, and the partially-porous 'Recemat' airfoils with various c_p/c from [9, 12]. The plot markers are described in Table 1. The face colors correspond to the different c_p/c, white means c_p/c = 1.

Outside the enlarged area, a poorer agreement of the fully-porous 'Recemat' (r = 8,200 Nsm^{-4}) and 'Damtec USM' (r = 12,900 Nsm^{-4}) airfoils to the $c_p/c = 1$ curve is found. This could be because for the low r, the assumption used in the formulation of Eqs. (2) and (5), which requires w_s to be small, no longer holds [13]. Therefore, one could expect the inherent mismatch between the prediction and the experimental results, when an attempt is made to predict the lift of porous airfoils with a relatively low air flow resistivity.

For partially-porous SD7003 airfoils, a high sensitivity of c_l drop is anticipated for the low values of c_p/c. In other words, when the porous extent of the airfoil is as small as 5% to 10% of the chord, a slight increase of the porous extent of 5% to 10% could result in a substantial drop of lift. However, when c_p/c increases by 20% from 30% to 50%, the drop of lift is not as large. The sensitivity of the c_l drop is, however, observed to behave slightly differently in the experimental data. A comparably-large c_l drop is observed when c_p/c changes from 0.05 to 0.1 and from 0.3 to 0.5, while there is only a relatively small drop of c_l for c_p/c between 0.1 and 0.3. Therefore, the sensitivity of c_l drop with the increasing porous extent for the low c_p/c values, which are of high interest for practical applications in reducing the turbulent boundary layer trailing-edge noise, may be overestimated by the thin-airfoil model. This over-prediction could be attributed to the drastic drop of $-p'(x)$ upstream of the porous extent discussed previously, which was not found to be the case, experimentally.

The comparison presented so far has shown that the thin-airfoil could correctly capture the trend of the lift coefficient reduction with the increasing porosity constant. A relatively closer agreement is found when the airfoil profile is close to a thin airfoil and the material's air flow resistivity is high, i.e. the imposed Darcy's boundary condition holds. Underestimation of lift could be found for partially-porous airfoils for a number of reasons. Apart from the deviations from the aforementioned assumed conditions, underprediction of lift could be caused by the overestimation of the pressure difference drop in the solid region upstream of the porous extent. Furthermore, inaccurate modelling of the material's effective air flow resistivity which is experienced by the flow when the material is integrated in the airfoil might also lead to prediction inaccuracies.

V. Conclusion

Fully- and partially-porous airfoils are capable of minimizing turbulent boundary trailing-edge noise. Nevertheless, the less lift force they produce makes them less desirable for real applications. An accurate tool which can predict pressure distribution on porous airfoils is important for designing an optimal integration of porous materials with the airfoil, for the maximum noise reduction and minimum aerodynamics penalty.

The recently-developed thin-airfoil approach for predicting steady pressure distribution on porous airfoil is assessed by comparing with experimentally-measured lift force data of full- and partially-porous airfoils. Use is made of the

available datasets of the thin and symmetric airfoil and the SD7003 airfoil, focusing on the partially-porous cases.

The most recent thin-airfoil formulation is able to handle airfoils with any arbitrary chordwise-differentiable porosity distribution. The no-slip boundary condition on the airfoil surface is replaced by the Darcy's boundary condition and solved as a Riemann-Hilbert problem. The PARSEC airfoil parameterization method is used to ensure an accurate representation of the airfoil geometry.

For the thin and symmetric partially-porous airfoil, the consistent drop of the lift curve slope with the increasing chordwise porous extent ratio (c_p/c) is accurately predicted by the thin airfoil. For relatively low porosity values, the lift is predicted to drop drastically with the increasing porosity. This is likely to be due to the underestimation of the pressure above the solid extent upstream of the porous extent, which is not found to be the case, experimentally. This phenomenon could cause underprediction of lift. For the relatively high porosity values, the lift reduction becomes less sensitive to the increasing porosity, and the source of lift loss is found to be mainly from around the porous extent of the airfoil itself.

Comparison of the pressure distribution on a solid SD7003 airfoil with the solution from the panel method in XFOIL shows the inherent inaccuracy of the thin-airfoil approach when used with a relatively thick airfoil due to the airfoil's geometry representation that uses only the camber line. Inaccurate prediction can be expected in regions with high surface curvature and/or thickness. For fully-porous SD7003 airfoils, accurate prediction of lift reduction is found for porous materials with relatively high air flow resistivities. This is because they satisfy the assumption in the Darcy's boundary condition.

For partially-porous airfoil, the model suggests a lower lift loss sensitivity to the increasing porosity of the localized porous material, which agrees well with the recent experimental finding. However, particularly for the partially-porous SD7003 airfoil, the model tends to overestimate the sensitivity of lift loss with the increasing c_p/c at the low chordwise extent ratios of approximately 5 to 30 percent, compared to the experimental data. This could be due to the aforementioned overestimation of the pressure drop on the solid extent upstream of the porous region.

Future work has been planned to investigate pressure distribution on porous airfoils using a numerical method, namely, the mimetic spectral element method (MSEM), to solve the Darcy problem. The full geometry of the airfoil is taken into account, and more freedom to model the materials is possible through the usage of the permeability tensor. It is also planned to compare the prediction with a dedicated experimental dataset.

Appendix

The 'PARSEC' airfoil parameterization method [19] is used in this work to parameterize the SD7003 airfoil's shape. The method has been developed by Sobieczky exclusively for airfoil design [31–33]. It requires 11 design variables to describe the geometric features of an airfoil. Then the design variables are used to construct systems of linear equations to solve for 12 polynomial coefficients. The polynomial coefficients are incorporated in two explicit polynomial equations for describing the airfoil's curvatures of the suction and the pressure sides.

The main reason why the PARSEC method is preferred for this work is because of the explicit, yet simple and differentiable polynomial equation it employs to describe the airfoil surface. The continuous and differentiable properties of the airfoil's geometry description are required by the thin-airfoil approach of Hajian and Jaworski [15], and also in the mimetic spectral element method (MSEM) [34] which makes use of the transfinite mapping method [35] for interpolation along arbitrary curves. The MSEM method will also be implemented in the upcoming work for predicting pressure distribution on porous airfoils.

Let $\mathbf{p} = \begin{bmatrix} p_1 & p_2 & p_3 & \dots & p_{11} \end{bmatrix}^T$ be a vector containing the geometric features of an arbitrary airfoil, the geometrical meanings of each element in $\mathbf{p}$ are depicted in the schematic in Fig. 7 and explained in Table 3. The vector $\mathbf{p}$ for the SD7003 airfoil are obtained iteratively, based on the point cloud of the actual SD7003 airfoil [36]. The values of each element in $\mathbf{p}$ for the SD7003 airfoil used in this work are given also in Table 3.

The elements in $\mathbf{p}$ are then incorporated in two systems of linear equations to solve for the polynomial coefficient vectors $\mathbf{a}_P$ and $\mathbf{a}_S$, used in the polynomial curves of the pressure side (lower surface) and suction side (upper surface), respectively. The systems of linear equations read [32, 37]:

$$\mathbf{C}_P\mathbf{a}_P = \mathbf{b}_P \qquad \mathbf{C}_S\mathbf{a}_S = \mathbf{b}_S, \tag{13}$$

where

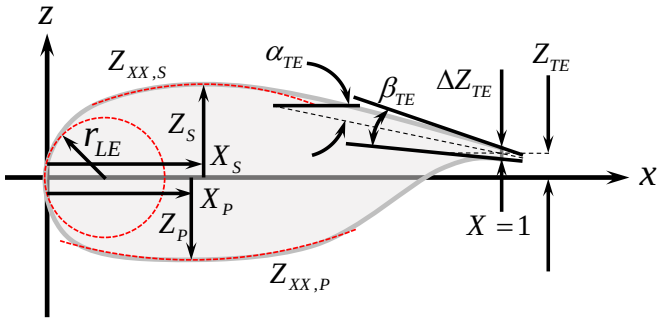

Fig. 7 Schematic of the PARSEC airfoil parameterization and its associating design variables (adapted from [19]).

Table 3 Descriptions of the PARSEC airfoil design variables and the corresponding values used for parameterizing the SD7003 airfoil (adapted from [37]).

Variable	Symbol	Description	SD7003 value
p_1	r_{LE}	Leading-edge radius	0.0130
p_2	X_S	Upper crest position in horizontal coordinates	0.2876
p_3	Z_S	Upper crest position in vertical coordinates	0.0566
p_4	$Z_{XX,S}$	Upper crest curvature	-0.3951
p_5	X_P	Lower crest position in horizontal coordinates	0.2127
p_6	Z_P	Lower crest position in vertical coordinates	-0.0290
p_7	$Z_{XX,P}$	Lower crest curvature	0.2602
p_8	Z_{TE}	Trailing-edge offset	0
p_9	ΔZ_{TE}	Trailing-edge thickness	0
p_{10}	α_{TE}	Trailing-edge direction	-1.7939
p_{11}	β_{TE}	Trailing-edge wedge angle	3.5879

$$\mathbf{b}_P = \begin{bmatrix} p_8 - p_9/2 \\ p_6 \\ \tan(p_{10} + p_{11}/2) \\ 0 \\ \dfrac{p_7}{\sqrt{2p_1}} \end{bmatrix} \qquad \mathbf{b}_S = \begin{bmatrix} p_8 + p_9/2 \\ p_3 \\ \tan(p_{10} - p_{11}/2) \\ 0 \\ \dfrac{p_4}{\sqrt{2p_1}} \end{bmatrix}, \tag{14}$$

and

$$\mathbf{C}_S = \begin{bmatrix} 1 & 1 & 1 & 1 & 1 & 1 \\ p_2^{1/2} & p_2^{3/2} & p_2^{5/2} & p_2^{7/2} & p_2^{9/2} & p_2^{11/2} \\ 1/2 & 3/2 & 5/2 & 7/2 & 9/2 & 11/2 \\ \frac{1}{2}p_2^{-1/2} & \frac{3}{2}p_2^{1/2} & \frac{5}{2}p_2^{3/2} & \frac{7}{2}p_2^{5/2} & \frac{9}{2}p_2^{7/2} & \frac{11}{2}p_2^{11/2} \\ -\frac{1}{4}p_2^{-3/2} & \frac{3}{4}p_2^{-1/2} & \frac{15}{4}p_2^{1/2} & \frac{35}{4}p_2^{3/2} & \frac{63}{4}p_2^{5/2} & \frac{99}{4}p_2^{7/2} \\ 1 & 0 & 0 & 0 & 0 & 0 \end{bmatrix}. \tag{15}$$

Formulation of $\mathbf{C}_P$ is done in the same fashion as $\mathbf{C}_S$ in Eq. (15), replacing p_2 by p_5.

Finally, the local surface coordinates z_P and z_S for any given dimensionless chordwise distance $x \in [0, 1]$ is obtained from the dedicated polynomial equations [19]:

$$z_P = \sum_{i=1}^{6} a_{P,i} x^{i-\frac{1}{2}} \qquad z_S = \sum_{i=1}^{6} a_{S,i} x^{i-\frac{1}{2}}. \tag{16}$$

For the SD7003 airfoil, the elements of the vectors $\mathbf{a}_P$ and $\mathbf{a}_S$ used are given in Table 4. Correspondingly, the curves representing the airfoil's shape from Eq. (16) compared to the point cloud of the SD7003 airfoil, the resulting airfoil's chordwise thickness distribution $d(x)$, and local slope of the camber line dz_a/dx, derived from the PARSEC parameterization method are shown in Figs 2a to 2c in the main text.

Table 4 Values of the PARSEC polynomial coefficients used for parameterizing the SD7003 airfoil.

Pressure side, $\mathbf{a}_P$	$a_{P,1}$	$a_{P,2}$	$a_{P,3}$	$a_{P,4}$	$a_{P,5}$	$a_{P,6}$
	-0.1162	0.4017	-0.9775	1.4384	-0.9077	0.1612
Suction side, $\mathbf{a}_S$	$a_{S,1}$	$a_{S,2}$	$a_{S,3}$	$a_{S,4}$	$a_{S,5}$	$a_{S,6}$
	0.1612	-0.1908	-0.0885	0.4007	-0.5161	0.2335

Acknowledgments

- This work is a part of the Innovative PERmeable Materials for Airfoil Noise Reduction (IPER-MAN) project funded by the Netherlands Organisation for Scientific Research (NWO) and the associating users (Project number 15452).
- The authors would like to thank Dr. Thomas Geyer for providing the experimental data, and answering the questions regarding the data.
- The authors would like to thank Dr. Mohammed Aldheeb for answering the questions regarding the experimental set-up.
- The authors would like to acknowledge Dr. Marc Gerritsma and Varun Jain for the inspiring discussion regarding the MSEM method and the future collaboration.

References

[1] Brooks, T. F., Pope, D. S., and Marcolini, M. A., "Airfoil self-noise and prediction," 1989.

[2] Geyer, T., Sarradj, E., and Fritzsche, C., "Measurement of the noise generation at the trailing edge of porous airfoils," *Experiments in Fluids*, Vol. 48, No. 2, 2010, pp. 291–308.

[3] Lilley, G., "A study of the silent flight of the owl," *4th AIAA/CEAS Aeroacoustics Conference*, 1998, p. 2340.

[4] Rubio Carpio, A., Merino Martinez, R., Avallone, F., Ragni, D., Snellen, M., and van der Zwaag, S., "Broadband Trailing-Edge Noise Reduction Using Permeable Metal Foams," *INTER-NOISE and NOISE-CON Congress and Conference Proceedings*, Vol. 255, Institute of Noise Control Engineering, 2017, pp. 2755–2765.

[5] Rubio Carpio, A., Merino Martínez, R., Avallone, F., Ragni, D., Snellen, M., and van der Zwaag, S., "Experimental characterization of the turbulent boundary layer over a porous trailing edge for noise abatement," *Journal of Sound and Vibration*, Vol. 443, 2019, pp. 537–558.

[6] Herr, M., "Design criteria for low-noise trailing-edges," *13th AIAA/CEAS Aeroacoustics Conference (28th AIAA Aeroacoustics Conference)*, 2007, p. 3470.

[7] Geyer, T., Sarradj, E., and Fritzsche, C., "Porous airfoils: noise reduction and boundary layer effects, 15th AIAA," *CEAS aeroacoustics conference, AIAA paper*, Vol. 3392, 2009.

[8] Sarradj, E., and Geyer, T., "Noise generation by porous airfoils," *13th AIAA/CEAS Aeroacoustics Conference (28th AIAA Aeroacoustics Conference)*, 2007, p. 3719.

[9] Geyer, T. F., and Sarradj, E., "Self Noise Reduction and Aerodynamics of Airfoils With Porous Trailing Edges," *Acoustics*, Vol. 1, Multidisciplinary Digital Publishing Institute, 2019, pp. 393–409.

[10] Herr, M., Rossignol, K.-S., Delfs, J., Lippitz, N., and Mößner, M., "Specification of porous materials for low-noise trailing-edge applications," *20th AIAA/CEAS aeroacoustics conference*, 2014, p. 3041.

[11] Geyer, T. F., and Sarradj, E., "Trailing edge noise of partially porous airfoils," *20th AIAA/CEAS Aeroacoustics Conference*, 2014, p. 3039.

[12] Geyer, T., and Sarradj, E., "Noise reduction and aerodynamics of airfoils with porous trailing edges," *INTER-NOISE and NOISE-CON Congress and Conference Proceedings*, Vol. 258, Institute of Noise Control Engineering, 2018, pp. 641–650.

[13] Aldheeb, M., Asrar, W., Sulaeman, E., and Omar, A. A., "Aerodynamics of porous airfoils and wings," *Acta Mechanica*, Vol. 229, No. 9, 2018, pp. 3915–3933.

[14] Mößner, M., "Volume-Averaged RANS-Simulation of Turbulent Flow over Porous Media," Ph.D. thesis, PhD thesis, TU Braunschweig, Institut für Strömungsmechanik, 2016.

[15] Hajian, R., and Jaworski, J. W., "The steady aerodynamics of aerofoils with porosity gradients," *Proc. R. Soc. A*, Vol. 473, No. 2205, 2017, p. 20170266.

[16] Bae, Y., and Moon, Y. J., "Effect of passive porous surface on the trailing-edge noise," *Physics of Fluids*, Vol. 23, No. 12, 2011, p. 126101.

[17] Iosilevskii, G., "Aerodynamics of permeable membrane wings," *European Journal of Mechanics-B/Fluids*, Vol. 30, No. 5, 2011, pp. 534–542.

[18] Iosilevskii, G., "Aerodynamics of permeable membrane wings. Part 2: Seepage drag," *European Journal of Mechanics-B/Fluids*, Vol. 39, 2013, pp. 32–41.

[19] Sobieczky, H., "Parametric airfoils and wings," *Recent development of aerodynamic design methodologies*, Springer, 1999, pp. 71–87.

[20] Muskhelishvili, N. I., and Radok, J. R. M., *Singular integral equations: boundary problems of function theory and their application to mathematical physics*, Courier Corporation, 2008.

[21] Dow, M., and Elliott, D., "The Numerical Solution of Singular Integral Equations over (-1,1)," *SIAM Journal on Numerical Analysis*, Vol. 16, No. 1, 1979, pp. 115–134.

[22] Drela, M., *Flight vehicle aerodynamics*, MIT press, 2014.

[23] Tian, Z., "The Steady Aerodynamics of Airfoils with Uniform Porosity," 2014.

[24] Darcy, H., *Les fontaines publiques de la ville de Dijon: exposition et application...*, Victor Dalmont, 1856.

[25] Ingham, D. B., and Pop, I., *Transport phenomena in porous media*, Elsevier, 1998.

[26] von Schulz-Hausmann, F. K., "Wechselwirkung ebener Freistrahlen mit der Umgebung," *Forschung im Ingenieurwesen*, Vol. 52, No. 2, 1986, pp. 56–56.

[27] "ISO 9053: Acoustics—Materials for acoustical applications—Determination of airflow resistance," , 1991.

[28] Ergun, S., and Orning, A. A., "Fluid flow through randomly packed columns and fluidized beds," *Industrial & Engineering Chemistry*, Vol. 41, No. 6, 1949, pp. 1179–1184.

[29] Li, L., and Ma, W., "Experimental study on the effective particle diameter of a packed bed with non-spherical particles," *Transport in porous media*, Vol. 89, No. 1, 2011, pp. 35–48.

[30] Drela, M., "XFOIL: An analysis and design system for low Reynolds number airfoils," *Low Reynolds number aerodynamics*, Springer, 1989, pp. 1–12.

[31] Hajek, J., "Parameterization of airfoils and its application in aerodynamic optimization," *WDS*, Vol. 7, 2007, pp. 233–240.

[32] Zhu, F., Qin, N., Burnaev, E., Bernstein, A., and Chernova, S., "Comparison of three geometric parameterization methods and their effect on aerodynamic optimization," *Eurogen*, 2011, pp. 758–772.

[33] Salunke, N. P., Juned Ahamad, R., and Channiwala, S., "Airfoil parameterization techniques: A review," *American Journal of Mechanical Engineering*, Vol. 2, No. 4, 2014, pp. 99–102.

[34] Gerritsma, M., Palha, A., Jain, V., and Zhang, Y., "Mimetic Spectral Element Method for Anisotropic Diffusion," *Numerical Methods for PDEs*, Springer, 2018, pp. 31–74.

[35] Gordon, W. J., and Hall, C. A., "Transfinite element methods: blending-function interpolation over arbitrary curved element domains," *Numerische Mathematik*, Vol. 21, No. 2, 1973, pp. 109–129.

[36] "UIUC Airfoil Coordinate Database," `https://m-selig.ae.illinois.edu/ads/coord_database.html`, 1995. Accessed: 2019-04-22.

[37] Della Vecchia, P., Daniele, E., and DAmato, E., "An airfoil shape optimization technique coupling PARSEC parameterization and evolutionary algorithm," *Aerospace Science and Technology*, Vol. 32, No. 1, 2014, pp. 103–110.